eprints@whiterose.ac.uk
https://eprints.whiterose.ac.uk/

Investigation of Scaling Effect on Power Factor of Permanent Magnet Vernier Machines for Wind Power Application

D. K. Kana Padinharu[1], G. J. Li [1*], Z. Q. Zhu[1], R. Clark[2], Z. Azar[2], and A. Thomas[2]

[1] Department of Electronic and Electrical Engineering, The University of Sheffield, Sheffield, UK
[2] Siemens Gamesa Renewable Energy Limited, North Campus, Broad Lane, Sheffield, UK
[*] g.li@sheffield.ac.uk.

Abstract: This paper investigates the scaling effect on power factor of surface mounted permanent magnet Vernier (SPM-V) machines with power ratings ranging from 3kW, 500kW, 3MW to 10MW. For each power rating, different slot/pole number combinations have been considered to study the influence of key parameters including inter-pole magnet leakage and stator slot leakage on power factor. A detailed analytical modelling, incorporating these key parameters, is presented and validated with 2D Finite Element Analysis (FEA) for different power ratings and slot/pole number combinations. The study has revealed that with scaling (increasing power level), significant increase in electrical loading combined with the increased leakage fluxes, i.e. (a) magnet leakage flux due to large coil pitch to rotor pole pitch ratio, (b) magnet inter-pole leakage flux and (c) stator slot leakage flux, reduces the ratio of armature flux linkage to PM flux linkage and thereby has a detrimental effect on the power factor. Therefore, unlike conventional SPM machines, the power factor of SPM-V machines is found to be significantly reduced at high power ratings.

1. Introduction

Offshore wind power has huge potential to be one of the main renewable energy sources for electric power generation. Larger wind turbines can significantly reduce the overall cost of offshore wind farms, making the wind energy a competitive source of clean energy [1]. Because of the harsh environment, the reliability and maintenance have been major challenges for the offshore wind market. Gear box is considered to be one of the weakest link in the whole drive train system, creating serious reliability issues [2]. A direct drive system enables the complete elimination of the gearbox by directly coupling the generator with the shaft of turbine blades. However, high power at low speed equates to high torque and hence increases the volume and mass of the direct drive generators. Several solutions have been proposed in the past to improve direct drive machines torque/power density such as transverse flux machines [3], magnetically geared machines [4], [5] etc. However, these machines often have complicated structures, making them less attractive for high power applications.

Recently, Vernier machines, based on the same principle as magnetically geared machines [6], have become very popular mainly due to their high torque density combined with simple structure. In addition, its inherent low torque ripple makes it very suitable for low-speed direct drive applications [7], [8]. However, a relatively low power factor compared to conventional permanent magnet (PM) machines currently prevents its penetration into wider industrial applications [9]–[11] due to the requirement for larger converter ratings, which could lead to increase in system cost and losses. Several novel Vernier topologies have been proposed in the past to improve the power factor of such machines [12]–[15] to address this critical issue. However, the review of literature reveals that most of the works related to power factor improvement and its analysis have been performed for relatively small scale (up to few kWs) Vernier machines. Moreover, a systematic study of the impact of scaling on power factor has not been done before. Such study is critical due to the increasing power rating of offshore wind turbine.

In line with this objective, this paper presents a detailed study on the performance of conventional SPM-V machine (as shown in Fig. 1) over a wide range of power ratings (3kW to 10MW) compared to a conventional SPM machine with main focus on the power factor. Different slot/pole number combinations will be analyzed for each power rating to assess the optimal performance. In previous work, researchers have used simple power factor equations to qualitatively explain the poor power factor of SPM-V machines against the conventional SPM machines [6], [12], [15]–[17]. However, a detailed consideration of parameters like inter-pole magnet leakage and stator slot leakage fluxes across different slot/pole numbers for power factor calculation has not been performed before. Therefore, the consideration of these parameters in the power factor calculation and their quantitative validation with 2D FE analysis across power ratings and different slot/pole numbers adds to extra novelty of this work.
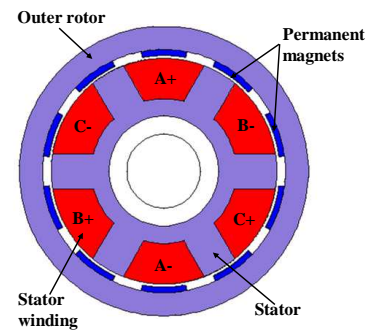
Fig. 1. An example of SPM-V machine topology with 6-slot/10-pole.

2. Basic working principle of Vernier machine

SPM-V machines, unlike conventional SPM machines, utilize the flux modulation principle for generating high torque [14], [15]. The stator open slot structure in Vernier machines (as shown in Fig. 1) modulates the rotor magnet MMF in the airgap, which can be calculated by [7]

$$F_{PM}(\theta_s, t) = \sum_{i=1,3,5\ldots}^{\infty} F_{PMi}\cos(iP_r\theta_s - i\omega_e t) \quad (1)$$

where P_r is the rotor pole pair number, ω_e is the rotor electrical speed, F_{PMi} is the amplitude of ith order MMF harmonics and θ_s is the angular position in the airgap with respect to stator reference. The airgap permeance created by the stator open slot structure is given by

$$\Lambda(\theta_s) = \Lambda_0 + \sum_{J=1,2,3\ldots}^{\infty} \Lambda_j \cos(jZ\theta_s) \qquad (2)$$

where Z is the number of stator slots, Λ_0 is the constant airgap permeance value and Λ_j is the amplitude of jth order harmonics of the permeance function. For simplicity, considering only the interaction between the fundamental magnet MMF (F_1) and the constant (Λ_0) as well as the first order (Λ_1) components of the airgap permeance, the airgap flux density $[B_g(\theta_s,t)]$ is given by [7], [19], [20]

$$
\begin{aligned}
B_g(\theta_s,t) = &B_{P_r}\cos(P_r\theta_s - \omega_e t) \\
&+ B_{z-P_r}\cos\big[((Z-P_r)\theta_s + \omega_e t)\big] \\
&+ B_{z+P_r}\cos\big[((Z+P_r)\theta_s - \omega_e t)\big]
\end{aligned}
$$

$$(3)$$

With

$$
\begin{cases}
B_{P_r} = F_1\Lambda_0 \\
B_{z-P_r} = \dfrac{1}{2}F_1\Lambda_1 \\
B_{z+P_r} = \dfrac{1}{2}F_1\Lambda_1
\end{cases}
\qquad (4)
$$

where B_{P_r} is the fundamental airgap flux density, B_{z-P_r} and B_{z+P_r} are the modulated airgap flux densities, respectively. As the modulated airgap flux density generates the same electrical frequency as the fundamental, all of them can contribute to the induced EMF and therefore classified as working harmonics.

The subharmonic in the modulated airgap flux density, B_{z-P_r}, rotates at a speed of $[P_r/(Z-P_r)]$ times the rotor mechanical speed. This results in a fast changing airgap field for a relatively small mechanical motion of the rotor enabling high torque for the SPM-V machines [18]. This is similar to a magnetic gearing effect wherein a high speed is generated from a low speed rotary motion. The ratio of this high speed modulated airgap field to the low rotor mechanical speed is defined as the gear ratio (G_r) of the SPM-V machine and is given by $G_r = P_r/(Z-P_r)$. To maximize the utilization of this high-speed low pole pair ($Z-P_r$) subharmonic component, the stator is wound for the same modulated pole pair. Therefore, the slot/pole number combination of the SPM-V machines follows a specific rule described by

$$P_r = Z - P_s \text{ or } P_r = Z + P_s \qquad (5)$$

where P_s is the stator winding pole pair number. It has been proven that the Vernier machine designed with slot/pole number combination given by $P_r = Z - P_s$ enables higher torque compared to the one using the alternative ($P_r = Z + P_s$) [18]. Therefore, $P_r = Z - P_s$ is used throughout this paper for maximizing the torque capability. For this slot/pole number combination, the gear ratio can be represented as the ratio of rotor pole pair number to stator winding pole pair number, i.e. $G_r = P_r/(Z-P_r) = P_r/(P_s)$.

To produce higher torque than a conventional SPM machine, the SPM-V machine utilizes higher gear ratio. Therefore, with the same stator structure as the conventional SPM machine, an SPM-V machine will often have the following geometric features:

- Large rotor pole pair number
- Large coil pitch to rotor pole pitch ratio

Large rotor pole pair number results in a proportionately higher inter-pole magnet leakage compared to the total flux per pole. Many of the previous studies have correlated the poor power factor of the Vernier machine to this inter-pole magnet leakage [21]. However, it has been observed that there is a significant proportion of magnet flux that crosses the airgap, traverses through the stator back iron yet still does not contribute to the induced EMF. This major leakage is due to the large stator coil pitch to rotor pole pitch ratio utilized by Vernier machines to produce high torque by modulation effect [12]. These PM leakage fluxes will be investigated in detail in the following section.

3. Analytical modelling of power factor

As in conventional SPM machines and to simplify the calculation of power factor, it is reasonable to neglect the voltage drop due to armature resistance [14] and thereby expressing the power factor (PF) as

$$PF = \frac{E_{ph}}{\sqrt{E_{ph}^2 + (I_{ph}X_{ph})^2}} = \frac{1}{\sqrt{1 + \left(\frac{I_{ph}X_{ph}}{E_{ph}}\right)^2}} \qquad (6)$$

where I_{ph} is the armature current, E_{ph} is the induced EMF, X_{ph} is the phase reactance. The power factor can be rewritten using the armature (Ψ_A) and permanent magnet (Ψ_{PM}) flux linkages as

$$PF = \frac{1}{\sqrt{1 + \left(\frac{I_{ph}L\omega_e}{T_{ph}\phi_{PM}\omega_e}\right)^2}} = \frac{1}{\sqrt{1 + \left(\frac{\Psi_A}{\Psi_{PM}}\right)^2}} \qquad (7)$$

where L is the synchronous inductance, ω_e is the electrical angular frequency, T_{ph} is the series turns per phase and ϕ_{PM} is the magnet flux per coil pitch. The power factor of the SPM-V machine depends on the ratio of armature flux linkage to PM flux linkage. The lower this ratio, the higher the power factor.

The following steps are involved in the derivation and validation of the analytical model for power factor:
(a) Analytical model and FE validation for PM flux linkage incorporating PM leakage fluxes developed in [22].
(b) Analytical model and FE validation for armature flux linkage incorporating the stator slot leakage flux.
(c) Combining the above two steps to obtain the ratio of armature flux linkage to PM flux linkage for derivation of power factor equation.
(d) Validation of power factor equation and studying the impact of scaling on performance of the SPM-V machines

3.1. Open circuit PM flux linkage

The calculation of open circuit induced EMF (E_{ph-v}) considering the inter-pole leakage flux is presented in [22] for an integer slot SPM-V machine as

$$E_{ph-v} = \frac{k_w T_{ph}\omega_m D_g L_{stk} B_{P_r} K_{fl}}{\sqrt{2}}\left(\frac{G_r^2}{(2G_r+1)}\Lambda_r + 1\right) \qquad (8)$$

where k_w is the fundamental winding factor, T_{ph} is the number of series turns per phase, ω_m is the rotor mechanical

2

angular velocity, D_g and L_{stk} are the airgap diameter and the stack length, respectively. Λ_r is defined as the ratio of Λ_1 to Λ_0. The inter pole leakage factor (K_{fl}) is given by [22]

$$K_{fl} = \frac{\tau_r - 2g}{\tau_r} \qquad (9)$$

where τ_r is the rotor pole pitch and g is the mechanical air gap length as shown in **Fig. 2**.

The induced EMF in (8) is essentially derived from the peak flux calculated by integrating the airgap flux density [see (3)] working harmonics over one coil pitch. It is worth noting that the integration of the fundamental airgap flux density (B_{P_r}) with P_r pole pair over the large coil pitch (as shown in Fig. 2) already takes into account the leakage flux due to large coil pitch to magnet pole pitch ratio (discussed in section 2). Therefore, (8) incorporates the inter-pole leakage flux and the leakage flux due to large coil pitch to rotor pole pitch ratio. The peak value of phase open-circuit flux linkage can be derived from (8) as expressed by

$$\Psi_{PM} = \frac{2}{\pi} k_w T_{ph} \tau_r L_{stk} B_{P_r} K_{fl} \left(\frac{G_r^2}{(2G_r + 1)} \Lambda_r + 1 \right) \qquad (10)$$
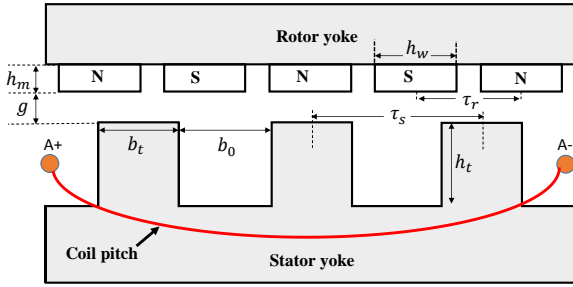
Fig. 2. Schematic of one pole model of an SPM-V with a gear ratio 5 resulting in five magnet poles within one coil pitch of an integer slot winding.

3.2. Validation with 2D FEA

Four conventional SPM machines with power ratings of 3kW, 500kW [23], 3MW [24] and 10MW [25] are selected as both the reference design and to provide the specification for comparable SPM-V machines. The key parameters of these conventional SPM machines are highlighted in Table 1. An outer rotor topology similar to the one shown in Fig. 1 is adopted here for all the power ratings because of its suitability for low speed high torque direct drive applications [26]. For each power rating of conventional SPM machine, corresponding SPM-V machines with different slot/pole number combinations are obtained by following the rule, $P_r = (Z - P_s)$. A gear ratio of 5 has been selected for this study as this is a popular gear ratio widely used in literature [7], [10], [19], [27]–[29]. The different slot/pole number combinations derived for the SPM-V machines are shown in Table 3 (see Appendix 3). To enable a fair comparison between SPM and SPM-V machines, all the designs for each power rating are optimized using genetic algorithm for maximum torque with their rotor outer diameter, magnet volume, phase current and copper loss kept constant.

Table 1 Key parameters of SPM machine

	3kW	500kW	3MW	10MW
Rated speed(rpm)	170	32	15	10
Outer diameter(m)	0.426	2.195	5	10
Airgap length (mm)	0.5	2.15	5	10
Stack length(m)	0.1	0.55	1.2	1.8
Magnet volume(m³)	0.00041	0.0162	0.227	0.92
Phase current(Arms)	2.7	438	2694	8796
Electrical loading(AT/mm)	9.3	62.7	58.6	54.5
Turns/phase	720	161	56	32
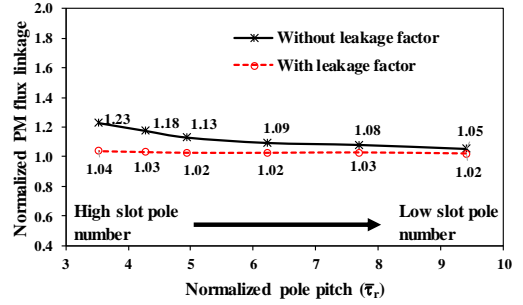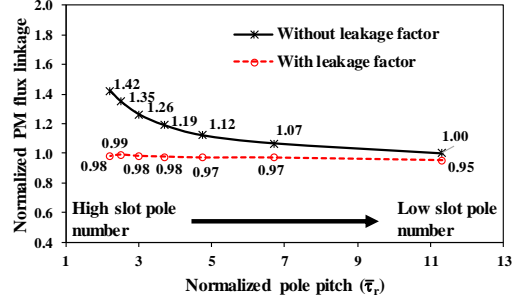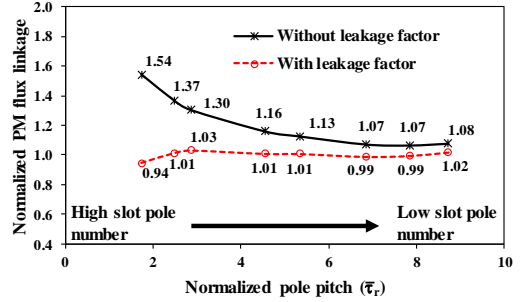
Fig. 3. Comparison of normalized PM flux linkage, with and without considering leakage factor, for different slot/pole number combinations of SPM-V machines at power ratings **(a)** 3kW, **(b)** 500kW, **(c)** 3MW, and **(d)** 10MW.

For a given power rating, the PM flux linkage of SPM-V machines varies significantly across different slot/pole numbers. Hence, a normalized value of flux linkage is u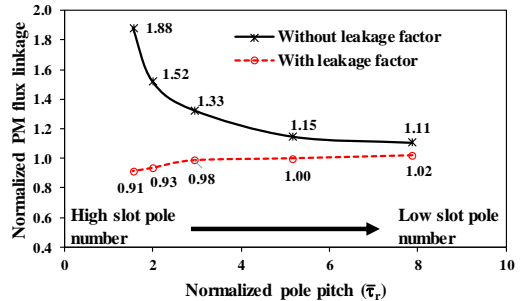sed here to compare the accuracy of the analytical equation [see (10)] and also to study the influence of leakage factor. The ratio of flux linkage calculated from analytical equation to that obtained by 2D FEA is defined as the normalized value for PM flux linkage. Further, to make the study more generic, the slot/pole numbers for different power ratings are expressed as normalized pole pitch ($\overline{\tau}_r$) which is defined as the ratio of pole pitch (τ_r) to magnetic airgap length (g') given by [22]

$$\overline{\tau}_r = \frac{\tau_r}{\left(g + \frac{h_m}{\mu_{rec}}\right)} = \frac{\tau_r}{g'} \qquad (11)$$

Table 2 Inter pole leakage factor (K_{fl}) calculated using (9) for different power ratings at various rotor pole pair numbers (P_r) of SPM-V machine

3kW		500kW		3MW		10MW	
P_r	K_{fl}	P_r	K_{fl}	P_r	K_{fl}	P_r	K_{fl}
20	0.967	35	0.952	40	0.944	60	0.919
30	0.952	70	0.908	50	0.931	100	0.869
40	0.936	105	0.865	60	0.919	200	0.741
60	0.907	140	0.821	80	0.894	300	0.613
80	0.877	175	0.777	100	0.868	400	0.484
100	0.847	210	0.733	160	0.792		

The leakage factors for SPM-V machines calculated using (9) for different power ratings are given in Table 2. The comparison of normalized PM flux linkage, with and without considering the leakage factor (K_{fl}) in (10), is shown in Fig. 3 for different power ratings across slot/pole numbers. The results clearly show that without the consideration of leakage factor, there is a significant difference between analytical predictions and 2D FEA results, particularly at high slot/pole number. This means that for high slot/pole number combinations, the inter-pole leakage flux becomes significant compared to the total flux per pole as shown in Fig. 4(b) and can result in reduced power factor. As expected, for SPM-V machines with low slot/pole number, the inter-pole leakage is negligible compared to the flux per pole, as shown in Fig. 4(a).
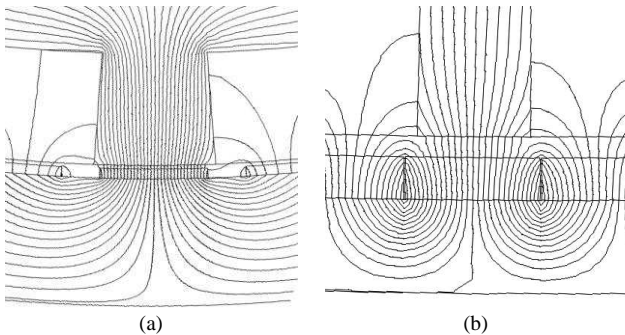

(a)   (b)

Fig. 4. Open circuit flux distribution with one magnet aligned with the stator tooth for the 500kW SPM-V machine with slot/pole number
(a) $N_s = 42, P_r = 35, P_s = 7$, **(b)** $N_s = 294, P_r = 245, P_s = 49$.
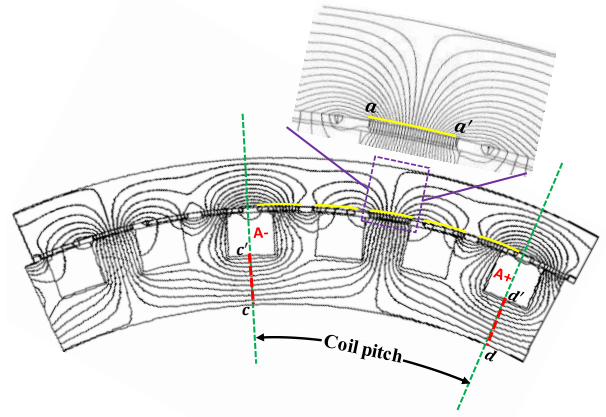

Fig. 5. Open circuit flux distribution for 500kW SPM-V machine with phase A having the maximum flux linkage.

However, it is observed that even for a low slot/pole number with negligible inter-pole leakage flux, the proportion of PM flux resulting in induced EMF is still significantly less compared to the total flux generated by the five magnets under one coil pitch. To verify this, open-circuit fluxes are extracted using 2D FEA as shown in Fig. 5. The 500kW SPM-V machine is used as example, and the rotor position is where the phase A has its maximum flux linkage. The total PM flux contributed by the 5 magnets under one coil pitch (ϕ_{PM_tot}) is obtained by summing the fluxes extracted from the bottom face of these magnets (yellow solid lines in Fig. 5). The flux contributing to the induced EMF (ϕ_{EMF}) is obtained by summing the flux extracted from cc' and dd' (red dotted line in Fig. 5). The difference of these two fluxes, ϕ_{PM_tot} and ϕ_{EMF}, is the total PM leakage flux per coil pitch (ϕ_{PMlkg_tot}). The inter-pole leakage flux contribution as a proportion of ϕ_{EMF} can be obtained from the analytical result shown in Fig. 3(b). Thereby, the two PM leakage fluxes, i.e. inter pole leakage flux (ϕ_{PMlkg_ip}) and the leakage flux (ϕ_{PMlkg_coil}) due to large coil pitch to rotor pole pitch, can be segregated. The comparison of these individual leakage fluxes for the 500kW SPM-V machine across slot/pole numbers is shown in Fig. 6. All the fluxes are presented as a normalized value with ϕ_{PM_tot} being the reference base value.
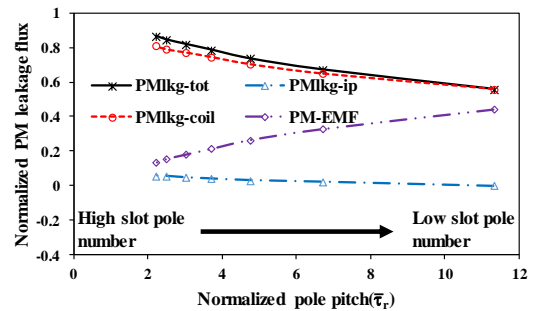
Fig. 6. Comparison of contribution of individual PM leakage fluxes to the total PM flux (ϕ_{PM_tot}) generated by the five magnets under one coil pitch across slot/pole number for the 500kW SPM-V machine.

The comparison reveals very interesting results that the total leakage flux at high slot/pole number ($\overline{\tau}_r \cong 2$) can reach almost 87% of the total PM flux (ϕ_{PM_tot}). And out of this, 80% is contribution from leakage flux due to large coil pitch to rotor pole pitch ratio (ϕ_{PMlkg_coil}). Although, the

4

inter-pole leakage flux at $\bar{\tau}_r \cong 2$ can be 42% of ϕ_{EMF}, it is still negligible compared to the ϕ_{PMlkg_coil}.

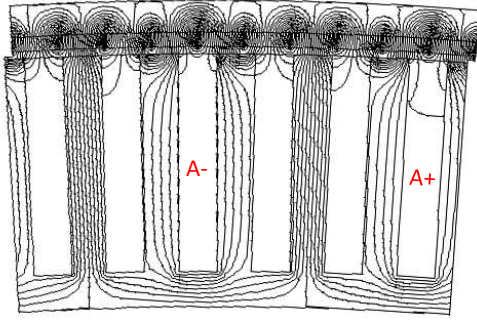**Fig. 7.** Contribution of inter-pole leakage flux and leakage flux due to large coil pitch.

The open-circuit flux distribution at $\bar{\tau}_r \cong 2$ for the 500kW SPM-V machine is shown in Fig. 7. It clearly shows the fact that compared to the total generated flux from the 5 magnets, significantly less fluxes are linking with the winding. For low slot/pole numbers, although the inter-pole leakage is negligible, ϕ_{PMlkg_coil} is almost 56% of ϕ_{PM_tot}. Thus, the study reveals that for Vernier machines, their PM leakage fluxes are largely dominated by the leakage flux due to large coil pitch. This is an inherent characteristic as they utilize the flux modulation or gearing effect to produce high torque. As a matter of fact, the higher the gear ratio is, the higher the coil pitch to rotor pole pitch ratio will be. This trend will lead to higher ϕ_{PMlkg_coil} resulting in even lower power factor.

4. Armature flux linkage calculation

In addition to the PM flux linkage, the power factor calculation also requires accurate prediction of the armature flux linkage. This section focuses on the derivation of an analytical equation for estimating the armature flux linkage considering the stator slot leakage flux, which is not negligible for a permanent magnet machine with a large magnetic airgap length.

4.1. Armature flux calculation

The armature flux distributions (without magnet excitation) in 500kW Vernier machines for a low $\bar{\tau}_r$ design ($\bar{\tau}_r = 2.2$) and a high $\bar{\tau}_r$ design ($\bar{\tau}_r = 6.7$) are shown in Fig. 8 (a) and (b), respectively. The flux distributions are shown at an instant when the phase C current is maximum. It is observed that for low $\bar{\tau}_r$ design, where the stator slot opening becomes comparable or lower than twice the magnetic airgap length (g'), there is significant amount of slot leakage flux [ϕ_3 in Fig. 8(a)]. For high $\bar{\tau}_r$ design, the slot leakage is negligible as the slot opening is much larger than $2g'$ and therefore almost all the fluxes (ϕ_1 and ϕ_2) cross the airgap. It is worth noting here that, the stator slot depth increases towards high slot/pole numbers to keep the copper loss constant.

A schematic of the armature flux distribution for one stator pole with three major flux paths (Loop1, Loop2 and Loop3 highlighted in red dotted lines) is shown in Fig. 9. Ampere's circuital law is applied to these three loops to

estimate the magnitudes of the armature fluxes. The following assumptions have been made for this calculation:

- The stator and rotor core are infinitely permeable.
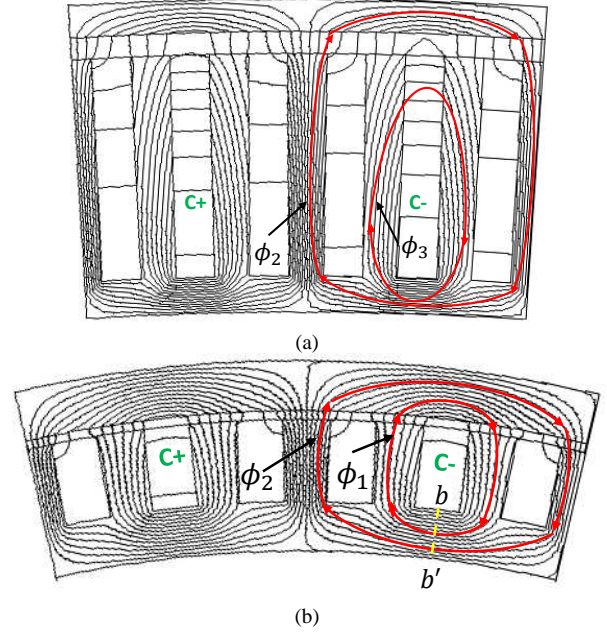- Airgap flux density is constant along the radial direction.

(a)

(b)

Fig. 8. Armature flux distribution (without magnet excitation) of the 500kW machine.
(a) $\bar{\tau}_r = 2.2$ with mainly two flux paths (ϕ_2, crossing the airgap and ϕ_3, slot leakage flux), **(b)** $\bar{\tau}_r = 6.7$ with mainly two flux paths (ϕ_1 and ϕ_2 both crossing the airgap).
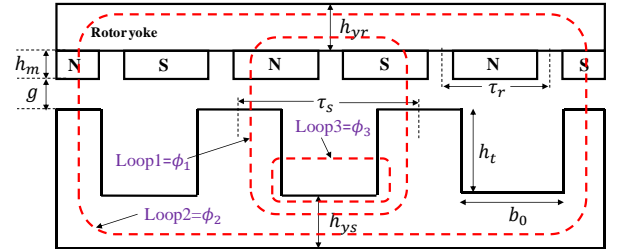

Fig. 9. Schematic showing three major flux loops (Loop1 carrying flux ϕ_1, Loop2 carrying flux ϕ_2 and Loop3 carrying flux ϕ_3) of armature flux distribution (no magnets excited).

Applying Ampere's circuital law, the fluxes in the three loops can be calculated as (see Appendix 1 for more detailed derivations)

$$\phi_1 = \frac{\sqrt{2}\mu_0}{m}\frac{G_r^2 \bar{\tau}_r \tau_r Q L_{stk}}{K_c(G_r + 1)} \tag{12}$$

$$\phi_2 = \frac{\sqrt{2}\mu_0}{m}\frac{G_r^2 \bar{\tau}_r \tau_r Q L_{stk}}{K_c(G_r + 1)} = \phi_1 \tag{13}$$

$$\phi_3 = \frac{\mu_0}{\sqrt{2}m}G_r \tau_r Q L_{stk}\left(\frac{h_t}{b_o}\right) \tag{14}$$

where Q is the electrical loading, m is the phase number, h_t is the stator slot height, b_o is the stator slot opening and $g'' = K_c\left(g + \frac{h_m}{\mu_{rec}}\right) = K_c g'$ is the effective airgap length, K_c is the Carter's coefficient given by [20], [30]

5

$$K_c = \left[1 - \frac{2}{\pi}\delta_s\left\{\tan^{-1}\left(\frac{b_o}{g'}\right) - \frac{g'}{b_o}\ln\left[1 + \frac{1}{4}\left(\frac{b_o}{g'}\right)\right]\right\}\right]^{-1} \quad (15)$$

(a)

(b)
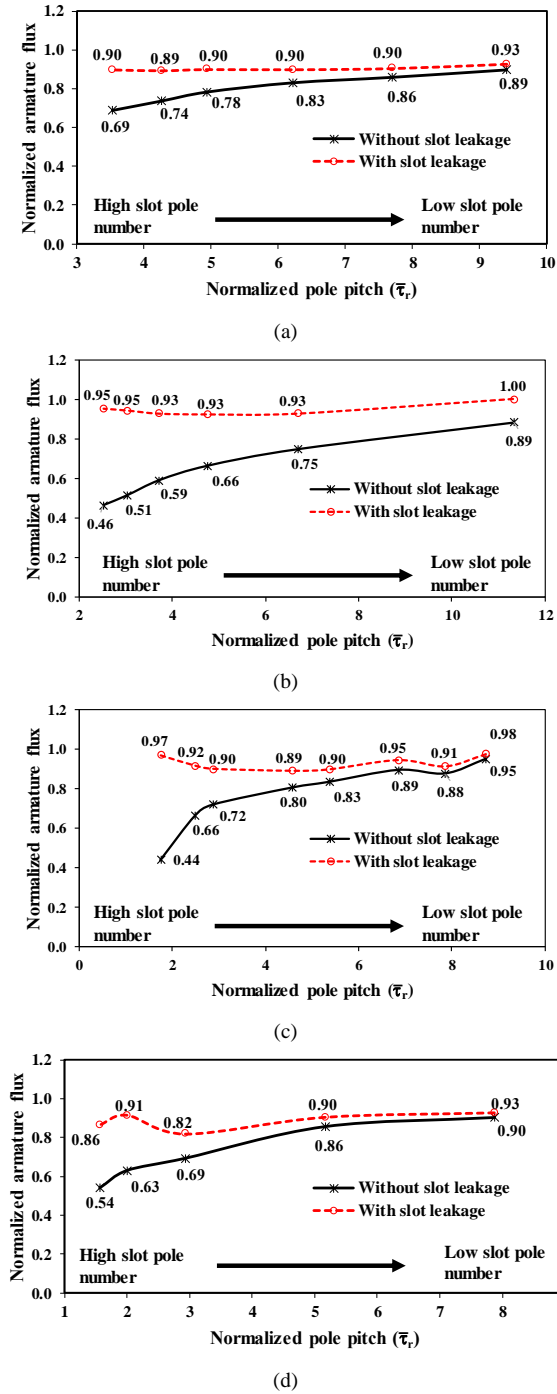
(c)

(d)

Fig. 10. Comparison of normalized armature flux, with and without considering the slot leakage flux, for SPM-V machine at power rating **(a)** 3kW **(b)** 500kW Vernier **(c)** 3MW and **(d)** 10MW.

It is worth noting here that the magnitudes of fluxes flowing in Loop1 and Loop2 are the same [see (12) and (13)]. For validating the armature flux calculation, total flux linking with the phase C is estimated directly by FEA by doubling the flux extracted from contour cc' [marked in yellow dotted line in Fig. 8(b)]. This value is then compared with the analytically calculated value wherein the total flux per coil pitch is expressed as $4\phi_1 + 2\phi_3$, where $2\phi_3$ is the slot

leakage flux contribution. The validation of the analytical armature fluxes for all the power ratings, with and without considering the slot leakage flux, is shown in Fig. 10. Similar to the PM flux linkage validation, the armature flux is represented as normalized value with their corresponding 2D FEA value as a base value.

The comparison shows that there is significant contribution from slot leakage flux to the total armature flux at high slot/pole number combinations where the slot width becomes comparable or less than twice of the magnetic airgap length. The slot leakage flux can be as high as 50% at a normalized pole pitch of around 2. Therefore, the consideration of this slot leakage flux is very important for accurate power factor calculation. Although the analytically predicted armature flux (considering the slot leakage flux) has almost ~10% deviation from 2D FEA, the error is nearly constant across various slot/pole numbers.

4.2. Armature flux linkage calculation

The armature flux linkage for the main flux $(4\phi_1)$ can be directly obtained by multiplying the number of turns per phase as the main flux crosses the airgap and loops around the entire turns per coil in the slot (see Fig. 9). Thus, the armature flux linkage (Ψ_{A_m}) for the main flux is given by

$$\Psi_{A_m} = T_{ph}(4\phi_1) = \frac{4\sqrt{2}\mu_0}{m}\frac{T_{ph}G_r^2\bar{\tau}_r\tau_r Q L_{stk}}{K_c(G_r + 1)} \quad (16)$$

However, for the slot leakage flux, the effective number of turns needs to be calculated to obtain the flux linkage. The schematic used for calculating the effective number of turns is shown in Fig. 11, which highlights the slot leakage flux loops around the conductors in a slot.
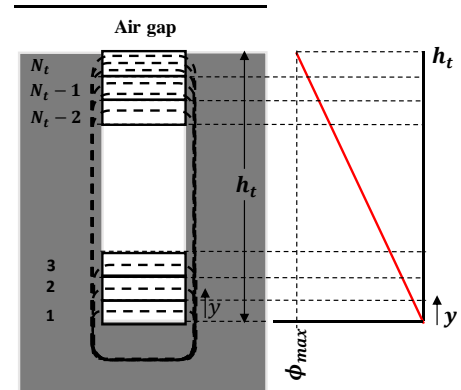
Fig. 11. The schematic showing stator slot leakage flux loops around the conductors in a slot. The coil in the slot with a slot height of h_t has a number of conductors N_t. The flux is assumed to be evenly distributed along the height of the slot in proportion to the enclosed current carrying conductors.

The schematic shows that the coil in the slot has a number of conductors (N_t) distributed evenly along the height of the slot (h_t). The magnitude of the flux in each loop is assumed to be proportional to the conductors enclosed by the loop. The variation of the magnitude of flux along the height of the slot is shown in Fig. 11, with ϕ_{max} being the maximum value contributed by N_t number of turns. The effective number of turns (out of N_t turns), N_{eff}, linking with the total

slot leakage flux ($2\phi_3$) can be calculated as (see Appendix 2 for more detailed derivation)

$$N_{eff} = \frac{(N_t + 1)(4N_t - 1)}{6N_t} \qquad (17)$$

Therefore, the total slot leakage flux linkage ($\Psi_{A_{sl}}$) per phase can be derived as

$$\Psi_{A_{sl}} = 2\phi_3 T_{ph} \frac{N_{eff}}{N_t} = \frac{\sqrt{2}\mu_0}{m} G_r \tau_r Q L_{stk} \left(\frac{h_t}{b_o}\right) T_{ph} \times \frac{N_{eff}}{N_t} \qquad (18)$$

5. Power factor calculation and validation

5.1. Power factor for different slot/pole numbers

The power factor equation can then be given as

$$PF = \frac{1}{\sqrt{1 + \left(\frac{\Psi_{A_m} + \Psi_{A_{sl}}}{\Psi_{PM}}\right)^2}} = \frac{1}{\sqrt{1 + (K_t)^2}} \qquad (19)$$

where K_t is the factor which represents the ratio of armature flux linkage to PM flux linkage. Substituting the values of PM and armature flux linkages from (10), (16) and (18), K_t can be expressed as

$$K_t = \left(\frac{\mu_0 \pi}{\sqrt{2}m}\right)\left(\frac{G_r Q}{B_{P_r}}\right) \frac{1}{K_{fl}(1 + K_{ver})}\left[\frac{4\overline{\tau}_r}{K_c}\left(\frac{G_r}{G_r + 1}\right) + \frac{h_t}{b_0}\frac{N_{eff}}{N_t}\right] \qquad (20)$$

where $K_{ver} = \frac{G_r^2}{(2G_r+1)}\Lambda_r$, representing the permeance term.

The following three scenarios have been included in the validation of the derived analytical equation to study the influence of each parameter on power factor. The equation for K_t corresponding to each scenario is also highlighted.

- Scenario 1: PM flux linkage without leakage factor (K_{fl}) and armature flux linkage without slot leakage flux ($2\phi_3$)

$$K_t = \left(\frac{2\sqrt{2}\mu_0 \pi}{m}\right)\left(\frac{G_r^2}{G_r + 1}\right)\left(\frac{Q}{B_{P_r}}\right)\left(\frac{\overline{\tau}_r}{K_c(1 + K_{ver})}\right) \qquad (21)$$

- Scenario 2: PM flux linkage with leakage factor and armature flux linkage without slot leakage flux

$$K_t = \left(\frac{2\sqrt{2}\mu_0 \pi}{m}\right)\left(\frac{G_r^2}{G_r + 1}\right)\left(\frac{Q}{B_{P_r}}\right)\left(\frac{\overline{\tau}_r}{K_c K_{fl}(1 + K_{ver})}\right) \qquad (22)$$

- Scenario 3: PM flux linkage with leakage factor and armature flux linkage with slot leakage flux [see (20)]

The impact of each scenario on the power factor calculation is compared across various slot/pole numbers at different power ratings, as shown in Fig. 12.
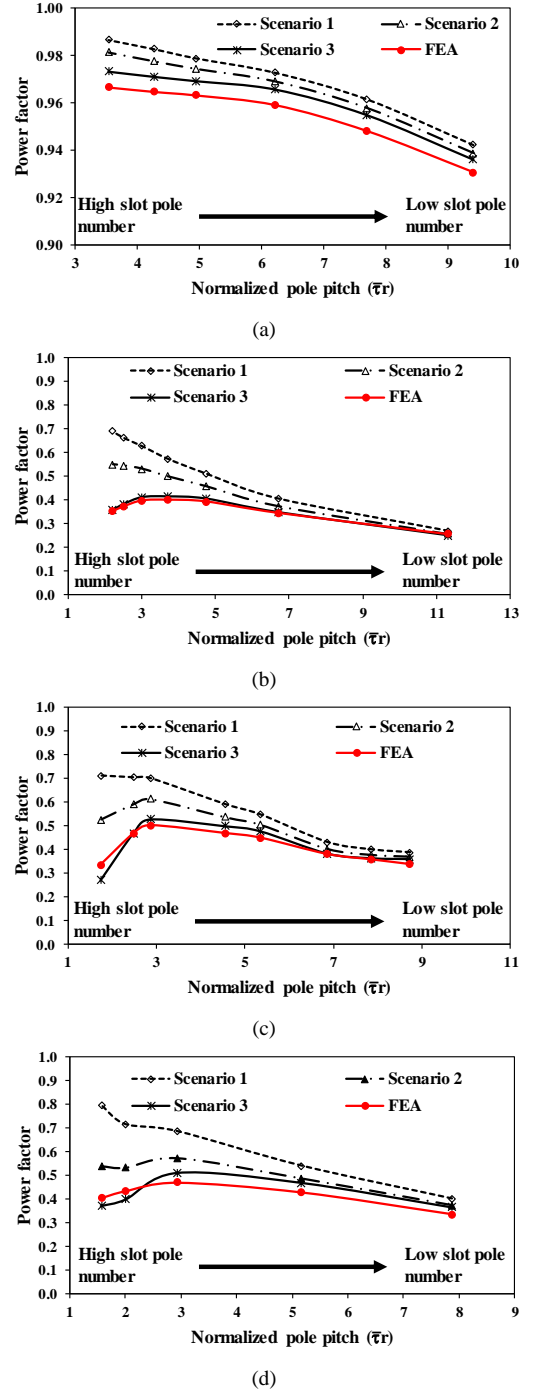

(a)

(b)

(c)

(d)

Fig. 12. Comparison of power factor calculation (with incremental improvements from Scenario 1 to Scenario 3) with 2D FEA across slot/pole number combinations at power ratings
(a) 3kW, **(b)** 500kW, **(c)** 3MW, and **(d)** 10MW.

The overall comparison shows that the power factor calculation using the analytical equation, incorporating the PM leakage factor (K_{fl}) and the armature slot leakage flux in Scenario 3, provides significantly better agreement with the FEA prediction. It also shows that the effect of these leakage fluxes on the power factor is significant, especially for higher slot/pole numbers. Interestingly, even though the PM inter-pole leakage flux is negligible compared to the leakage flux due to large coil pitch, they still have a significant impact on the value of power factor. This is because their magnitudes

become comparable to the flux linking with the winding as slot/pole number increases.

It is interesting to note here that the power factor shows an increasing trend (scenario 1) with higher slot/pole number when these leakage fluxes are neglected. This can be understood from (21). The last term in (21) represents the geometric parameter of the machine which is mainly a function of airgap permeance. The variation of this term, the ratio of $\overline{\tau_r}$ to $K_c(1 + K_{ver})$, is plotted against the normalized pole pitch for all power ratings and is shown in Fig. 13. For a given normalized pole pitch, this geometric term is observed to be almost the same across all power ratings and shows a decreasing trend with higher slot/pole numbers. The first three terms in (21) are almost constant across slot/pole numbers. Therefore, the power factor shows an increasing trend with higher slot/pole numbers for SPM-V machines. However, after the consideration of the PM leakage flux and armature stator slot leakage flux, this benefit in power factor at high slot/pole number disappears. This is particularly the case for higher power ratings. Although, at low slot/pole numbers, the inter-pole leakage flux and the slot leakage flux are negligible, the PM leakage flux due to large coil pitch still persists making the power factor poor for SPM-V machines.
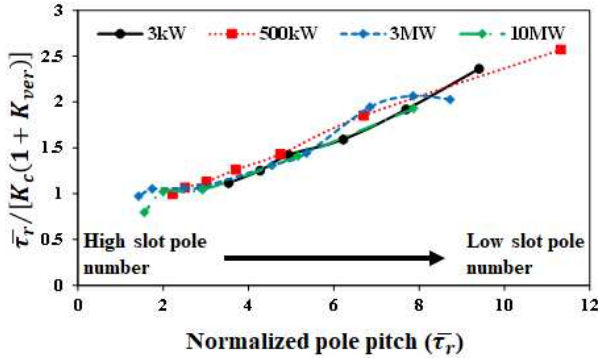

Fig. 13. Comparison of the term, $\overline{\tau_r}/[K_c(1 + K_{ver})]$, between different power ratings plotted against normalized pole pitch.

5.2. Scaling effect on power factor

For simplification, (21) has been considered to understand the trend of power factor with scaling (increasing power rating). The gear ratio ($G_r = 5$) is maintained the same for all power ratings. The last term, $\overline{\tau_r}/[K_c(1 + K_{ver})]$, is also found to be constant for a given $\overline{\tau_r}$. The magnetic loading (B_{P_r}) is not expected to change significantly across power ratings. Therefore, the power factor is directly proportional to the electrical loading (Q). The comparison of K_t between conventional SPM and SPM-V machines calculated from (21) as a function of electrical loading (for an assumed $\overline{\tau_r} = 3$) is shown in Fig. 14. The values of B_{P_r} and K_c are assumed to be 0.8T and 1.5, respectively. For the conventional SPM machine, $G_r = 1$ and $K_{ver} = 0$ has been used. It can be observed from Fig. 14 that the value of K_t for SPM-V machine increases with electrical loading at a much faster rate than conventional SPM machine. This is due to their high G_r value resulting in increased leakage due to a large coil pitch.

The power factors derived from their respective K_t using (19) are also shown in Fig. 14. For very low electrical loading (<10A/mm^2) K_t is observed to be much less than

unity for both conventional SPM and SPM-V machines. Therefore, the achievable power factors for both machines are almost near to unity. However, with increasing electrical loading, K_t for SPM-V machine can go beyond unity, leading to significantly reduced power factor, which is around 0.5. But for the conventional SPM machine, K_t is still much lower than 1, enabling it to achieve much higher power factor.
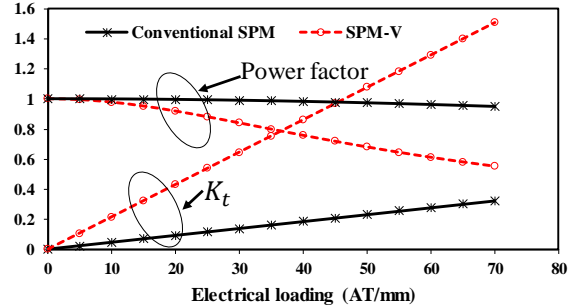

Fig. 14. Variation of K_t and power factor with electrical loading for $\overline{\tau_r} = 3$.

The comparison of power factor between the conventional SPM and SPM-V machines at different power ratings predicted by 2D FEA is shown in Fig. 15. As explained above, it is observed that the power factor of SPM-V machine drops significantly with increased rating. The 500kW SPM-V machine with the largest electrical loading shows the poorest power factor. However, the conventional SPM machine is able to give an acceptable high power factor across power ratings. The SPM-V machine with low electrical loading, e.g. the 3kW machine, is able to provide a high power factor (>0.9) comparable to that of the conventional SPM machine.
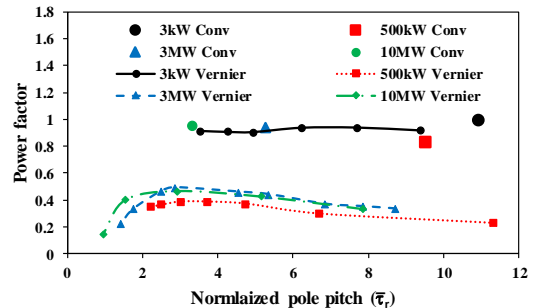
Fig. 15. Comparison of power factors (calculated using 2D FEA) between Vernier machines with power ratings of 3kW, 500kW, 3MW and 10MW.

5.3. Experimental Validation

The experimental validation for the 2D FEA model has been presented in the previous publication [22] which discussed a detailed analytical model for the induced EMF of the SPM-V machine. Two small prototypes (one for conventional SPM and one for SPM-V machine) have been tested and compared to validate the analytical and 2D FEA models. As this paper discusses a topic which is an extension of the previous publication [22], the test validation are assumed to be valid for the present work as well.

6. Conclusion

The impact of scaling on power factor of SPM-V machines is investigated using power ratings ranging from 3kW to 10MW. A detailed analytical modelling, incorporating the effects of all the leakage fluxes has been presented and validated. It has been revealed that SPM-V machines have an additional and significant PM leakage flux resulting from their large coil pitch to rotor pole pitch ratio which is absent in conventional SPM machines. This leakage flux together with the PM inter-pole and stator slot leakage fluxes reduce the power factor of SPM-V machines especially at high slot/pole numbers. Although leakage fluxes are high, negligible armature reaction at low power rating/electrical loading (~ <20AT/mm) enables SPM-V machines to achieve reasonably good power factor (> 0.9). However, at high power rating/electrical loading, the above mentioned leakage fluxes significantly reduce the power factor of SPM-V machines compared to conventional SPM machines.

7. Acknowledgment

8. Appendices

8.1. Appendix 1

Applying Ampere's circuital law to Loop1 (see Fig. 9), gives

$$\oint \vec{H}.\,\overline{dl} = N_t I_{ckt-pk} \tag{23}$$

where N_t is the number of turns per coil of stator winding and I_{ckt-pk} is the peak value of armature current. The peak value of radial airgap flux density (B_{gaL1}) along Loop1 is given by

$$B_{gaL1} = \frac{\mu_0 N_t I_{ckt-pk}}{2g''} \tag{24}$$

where

$$g'' = K_c \left(g + \frac{h_m}{\mu_{rec}}\right) = K_c g' \tag{25}$$

with

$$K_c = \left[1 - \frac{2}{\pi}\delta_s\left\{\tan^{-1}\left(\frac{b_o}{g'}\right) - \frac{g'}{b_o}\ln\left[1 + \frac{1}{4}\left(\frac{b_o}{g'}\right)\right]\right\}\right]^{-1} \tag{26}$$

The total flux in Loop1 can then be derived by integrating B_{gaL1} over one slot pitch (τ_s) as

$$\phi_1 = \frac{\mu_0 N_t I_{ckt-pk} L_{stk} \tau_s}{2g''} \tag{27}$$

N_t can be expressed in terms of turns per phase (T_{ph}), number of parallel branches (a) and stator winding pole pair (P_s) as

$$N_t = \frac{T_{ph} a}{P_s} \tag{28}$$

Applying

$$I_{ckt-pk} = \sqrt{2}I_{ph}/a \tag{29}$$

$$T_{ph}I_{ph} = \frac{\pi D_g Q}{2m} \tag{30}$$

$$\frac{\pi D_g}{2P_s} = G_r \tau_r \tag{31}$$

$$\tau_s = \frac{2G_r \tau_r}{(G_r + 1)} \tag{32}$$

We get

$$\phi_1 = \frac{\sqrt{2}\mu_0}{m} \frac{G_r^2 \overline{\tau}_r \tau_r Q L_{stk}}{K_c(G_r + 1)} \tag{33}$$

where I_{ph} is the phase current, Q is the electrical loading of the machine, m is the total number of phases.

Applying the same approach for Loop2, gives

$$\phi_2 = \frac{\sqrt{2}\mu_0}{m} \frac{G_r^2 \overline{\tau}_r \tau_r Q L_{stk}}{K_c(G_r + 1)} \tag{34}$$

Therefore, the magnitudes of flux flowing in Loop1 and Loop2 are the same.

Applying Ampere's circuital law in Loop3 and assuming a linear variation of ampere-turns in the coil, gives

$$\oint \vec{H}.\,\overline{dl} = N_t I_{ckt-pk}\frac{x}{h_t} \tag{35}$$

Assuming the whole MMF drop to be across the slot opening, the flux density in the stator slot (B_{gs}) can be calculated as

$$B_{gs} = \frac{\mu_0 N_t I_{ckt-pk}}{b_o}\left(\frac{x}{h_t}\right) \tag{36}$$

Integrating B_{gs} over the entire height of the slot (h_t) and length of the machine (L_{stk}) we get

$$\phi_3 = \mu_0 N_t I_{ckt-pk} L_{stk}\left(\frac{h_t}{2b_o}\right) \tag{37}$$

By following the same procedure as adopted for obtaining (33) from (27), ϕ_3 can be rewritten as

$$\phi_3 = \frac{\mu_0}{\sqrt{2}m} G_r \tau_r Q L_{stk}\left(\frac{h_t}{b_o}\right) \tag{38}$$

8.2. Appendix 2

The magnitude of the flux in each loop (see Fig. 11) is assumed to be proportional to the conductors enclosed by the loop. The variation of the magnitude of flux along the height of the slot is shown in Fig. 16, with ϕ_{max} being the maximum value contributed by N_t turns.
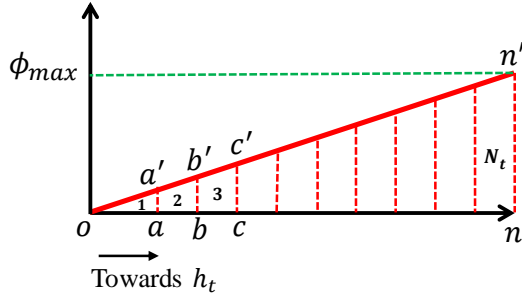
Fig. 16. Variation of flux magnitude from conductor 1 to N_t with ϕ_{max} being the maximum flux contributed by the N_t turns. Conductor 1 is placed first at the slot bottom.

The total slot leakage flux (ϕ_{sl}) contributed by all the conductors in one slot is given by the area under triangle onn'. The individual flux linkage with each conductor is calculated as below:

Conductor 1: Area under triangle oaa' multiplied by number of conductors within the area, given by

$$\frac{1}{2}\left(\frac{h_s}{N_t}\right)\left(\frac{\phi_{max}}{N_t}\right) \times 1 = \frac{\phi_{sl}}{N_t^2} \times 1 \tag{39}$$

Conductor 2: Area under trapezoid $aa'b'b$ multiplied by number of conductors within the area, given by

$$\left[\frac{1}{2}\left(2 \times \frac{h_s}{N_t}\right)\left(2 \times \frac{\phi_m}{N_t}\right) - \frac{1}{2}\left(1 \times \frac{h_s}{N_t}\right)\left(1 \times \frac{\phi_m}{N_t}\right)\right] \times 2$$
$$= \frac{\phi_{sl}}{N_t^2} \times 3 \times 2 \tag{40}$$

Extending this logic, the flux linkage with the final conductor N_t is given by

$$\frac{\phi_{sl}}{N_t^2} \times (2n-1)n \tag{41}$$

The total flux linkage is the summation of individual conductor flux linkage and is given by

$$\frac{\phi_{sl}}{N_t^2} \sum_{n=1}^{N_t} (2n-1)n = \phi_{sl} \times \frac{(N_t+1)(4N_t-1)}{6N_t} \tag{42}$$

8.3. Appendix 3

Table 3 Slot/pole number combinations investigated in this paper

Machine Type	Design number	3kW			500kW			3MW			10MW		
		N_s	P_r	P_s	N_s	P_r	P_s	N_s	P_r	P_s	N_s	P_r	P_s
Conventional	0	96	16	16	294	49	49	480	80	80	960	160	160
Vernier	1	24	20	4	42	35	7	48	40	8	48	40	8
Vernier	2	36	30	6	84	70	14	60	50	10	72	60	12
Vernier	3	48	40	8	126	105	21	72	60	12	120	100	20
Vernier	4	72	60	12	168	140	28	96	80	16	240	200	40
Vernier	5	96	80	16	210	175	35	120	100	20	480	400	80
Vernier	6	120	100	20	252	210	42	192	160	32	-	-	-
Vernier	7	-	-	-	294	245	49	240	200	40	-	-	-
Vernier	8	-	-	-	-	-	-	360	300	60	-	-	-
Vernier	9	-	-	-	-	-	-	480	400	80	-	-	-

9. References

[1] Poudineh, R., Brown, C., Foley, B.: 'Cost drivers and technical hurdles' in 'Economics of Offshore Wind Power: Challenges and Policy Considerations' (Palgrave Macmillan, 2017, 1st edn.), pp. 94.

[2] Koltsidopoulos Papatzimos, A., Dawood, T., Thies, P.: 'Data insights from an offshore wind turbine gearbox replacement', J. Phys. Conf. Ser., 2018, 1104.

[3] Tovar-Barranco, A., Gómez, D.J., López-de-Heredia, A., et al.: 'High torque density transverse flux permanent magnet machine design for wind power generation', in Proc. 22nd Int. Conf. Elect. Mach., 2016, pp. 782–788.

[4] Kjaer, A.B., Korsgaard, S., Nielsen, S.S., Demsa, L., et al.: 'Design, fabrication, test, and benchmark of a magnetically geared permanent magnet generator for wind power generation', IEEE Trans. Energy Convers., 2020, 35, (1), pp. 24–32.

[5] Zeinali, R., Keysan, O.: 'A rare-earth free magnetically geared generator for direct-drive wind turbines', Energies, 2019, 12, (3), pp. 447.

[6] Li, D.W., Qu, R.H., Li, J.: 'Topologies and analysis of flux-modulation machines', Proc. Energy Convers. Congr. Expo. (ECCE), 2015, pp. 2153–2160.

[7] Li, D.W., Qu, R.H., Li, J., et al.: 'Analysis of torque capability and quality in Vernier permanent-magnet machines', IEEE Trans. Ind. Appl., 2016, 52, (1), pp. 125–135.

[8] Okada, K., Niguchi, N., Hirata, K.: 'Analysis of a Vernier motor with concentrated windings', IEEE Trans. Magn., 2013, 49, (5), pp. 2241–2244.

[9] Jang, D.K., Chang, J.H.: 'Performance comparison of PM synchronous and PM Vernier machines based on equal output power per unit volume', J. Electr. Engin. Tech., 2016, 11, (1), pp. 150-156.

[10] Du, Z.S., Lipo, T.A.: 'Torque performance comparison between a ferrite magnet Vernier motor and an industrial interior permanent magnet machine', IEEE Trans. Ind. Appl., 2017, 53, (3), pp. 2088–2097.

[11] Oner, Y., Zhu, Z.Q., Chu, W.: 'Comparative study of Vernier and interior PM machines for automotive application," Proc. IEEE Vehicle Power Propuls. Conf., Hangzhou, China, 2016, pp. 1-6.

[12] Li, D., Qu, R., Lipo, T.A.: 'High-power-factor Vernier permanent-magnet machines', IEEE Trans. Ind. Appl., 2014, 50, (6), pp. 3664–3674.

[13] Xie, K.F., Li, D.W., Qu, R.H., et al.: 'A novel permanent magnet Vernier machine with halbach array magnets in stator slot opening', IEEE Trans. Magn., 2017, 53, (6), Art. no. 7207005.

[14] Ching, T.W., Chau, K.T., Li, W.: 'Power factor improvement of a linear Vernier permanent-magnet machine using auxiliary dc field excitation', IEEE Trans. Magn., 2016, 52, (7), pp. 1–4.

[15] Liu, Y., Li, H.Y., Zhu, Z.Q.: 'A high-power factor Vernier machine with coil pitch of two slot pitches', IEEE Trans. Magn., 2018, 54, (11), pp. 1–5.

[16] Kim, B., Lipo, T.A.: 'Operation and design principles of a PM Vernier motor', IEEE Trans. Ind. Appl., 2014, 50, (6), pp. 3656–3663.

[17] Kim, B.: 'Design method of a direct-drive permanent magnet Vernier generator for a wind turbine system', IEEE Trans. Ind. Appl., 2019, 55, (5), pp. 4665–4675.

[18] Toba, A., Lipo, T.A.: 'Generic torque-maximizing design methodology of surface permanent-magnet Vernier machine', IEEE Trans. Ind. Appl., 2000, 36, (6), pp. 1539–1546.

[19] Wu, L., Qu, R., Li, D., et al.: 'Influence of pole ratio and winding pole numbers on performance and optimal design parameters of surface permanent-magnet Vernier machines', IEEE Trans. Ind. Appl., 2015, 51, (5), pp. 3707–3715.

[20] Hyoseok, S., Niguchi, N., Hirata, K.: 'Characteristic analysis of surface permanent-magnet Vernier motor according to pole ratio and winding pole number', IEEE Trans. Magn., 2017, 53, (11), pp. 1–4.

[21] Li, W.L., Chau, K.T., Liu, C.H., et al.: 'Analysis of tooth-tip flux leakage in surface-mounted permanent magnet linear Vernier machines', IEEE Trans. Magn., 2013, 49, (7), pp. 3949–3952.

[22] Kana Padinharu, D.K., Li, G.J., Zhu, Z.Q., et al.: 'Scaling effect on electromagnetic performance of surface mounted permanent magnet Vernier machine', IEEE Trans. Magn., 2020, 56, (5), pp. 1–15.

[23] Grauers, A.: 'Design of direct driven permanent magnet generators for wind turbines', PhD thesis, Chalmers Univ. Technol., Goteborg, Sweden, 1996.

[24] Polinder, H., van der Pijl, F.F.A., de Vilder, G., et al.: 'Comparison of direct-drive and geared generator concepts for wind turbines', IEEE Trans. Energy Convers., 2006, 21, (3), pp. 725–733.

[25] Polinder, H., Bang, D., van Rooij, R., et al.: '10 MW wind turbine direct-drive generator design with pitch or active speed stall control', in Proc. IEEE IEMDC, Antalya, Turkey, 2007, 2, pp. 1390–1395.

[26] Yicheng, C., Pillay, P., Khan, A.: 'PM wind generator topologies', IEEE Trans. Ind. Appl., 2005, 41, (6), pp. 1619–1626.

[27] Zou, T., Li, D., Qu, R., et al.: 'Advanced high torque density PM Vernier machine with multiple working harmonics', IEEE Trans. Ind. Appl., 2017, 53, (6), pp. 5295–5304.

[28] Wu, L., Qu, L., Li, D.: 'Analysis of eddy current losses in surface-mounted permanent magnet Vernier machines', presented at the Proc. IEEE Int. Conf. Electr. Mach. Drives, 2017, pp. 1–6.

[29] Raza, M., Zhao, W.L., Lipo, T.A.: 'Performance comparison of dual airgap and single airgap spoke-type permanent-magnet Vernier machines', IEEE Trans. Magn., 2017, 53, (6), pp. 1–4.

[30] Zhu, Z.Q., Howe, D.: 'Instantaneous magnetic field distribution in brushless permanent magnet DC motors. III. Effect of stator slotting', IEEE Trans. Magn., 1993, 29, (1), pp. 143–151.

.